Journal of Natural Gas Science and Engineering 100 (2022) 104465

Contents lists available at ScienceDirect

Journal of Natural Gas Science and Engineering

journal homepage: www.elsevier.com/locate/jngse

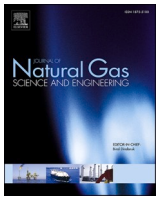

Effects of pressure control on droplet size distribution and flow regimes in gas–liquid cylindrical cyclone

Lele Yang [a], Lian Luo [a], Jing Wang [b], Jingyu Xu [c], Zhenfeng Zhai [b,*]

[a] School of Civil Engineering and Transportation, South China University of Technology, Guangzhou, 510641, PR China
[b] School of Marine Engineering and Technology, Sun Yat-sen University, Guangzhou, 510275, PR China
[c] Institute of Mechanics, Chinese Academy of Sciences, Beijing, 100190, China

ARTICLE INFO

Keywords:
Gas–liquid cylindrical cyclone
Flow regime
Dimensionless pressure
Pressure control
Droplet size

ABSTRACT

Marine production platforms and subsea production systems desperately need compact and highly efficient gas–liquid separators. The gas–liquid cylindrical cyclone (GLCC), which mainly utilizes gravitational and centrifugal forces to achieve separation, can be an superior choice. Herein, a pressure control scheme is proposed that allows the GLCC to realize fast and stable gas–liquid separation. The droplet size distributions measured by a Malvern RTSizer indicated that increasing the liquid superficial velocity only increased the distribution of small droplets at the inlet. The droplet size distribution of the down sampling at a high dimensionless pressure was larger than that at a low dimensionless pressure, which can be explained by the droplet migration model. As the dimensionless pressure decreased, four flow regimes were experimentally observed: annular flow, churn flow-stratified flow, falling droplets, and pure gas. Electrical resistance tomography measurement results indicated that better convergence of the bubbly filament was achieved at a higher dimensionless pressure.

1. Introduction

Gas and liquid separation is an essential step in offshore oil and gas production. Traditionally, conventional vessel-type separators relying on gravity and expansion have been employed for gas–liquid separation, as shown in Fig. 1. Owing to their large size, the cost of marine production platforms has increased significantly, and they are unsuitable for installation in subsea production systems (Saieed et al., 2018; Dalane et al., 2017). Therefore, it is imperative to develop compact, simple, and high-efficiency gas–liquid separators for the rapid development of marine oil and gas exploitation (Hreiz et al., 2011). The gas–liquid cyclone separator is an alternative to gravity separators.

Gas–liquid cyclone separators have different structures and can be divided into two types: axial inlet and tangent inlet. Cyclones with an axial inlet maintain the swirling flow via guide vanes; thus, they are also called vane-type separators. Their advantages of a compact structure and low flow resistance make them more suitable for space-limiting conditions (Cai et al., 2014; Chen et al., 2021; Niknam et al., 2018). However, their separation efficiency is not high, because the liquid always escapes from the gas stream emitted from the gas outlet (Yin et al., 2016, 2019). The most typical cyclone separator with a tangent inlet is the gas–liquid cylindrical cyclone (GLCC), which mainly utilizes gravitational and centrifugal forces to achieve gas–liquid separation (Moncayo et al., 2018). A GLCC is composed of a vertical pipe with a downward-inclined tangential inlet and two outlets: one for gas collection located at the top and another for liquid collection located at the bottom. The gas–liquid mixture flows into the GLCC via an inclined tangential inlet, and a vortex flow can be produced. Under gravity and centrifugal force, the liquid is pushed toward the pipe wall and discharges through the liquid leg, while the gas migrates to the center of the vertical pipe and is collected at the top outlet. The phenomenon in which the gas stream drags droplets or liquid film toward the gas outlet is called liquid carry-over (LCO) (Kolla et al., 2016). In gas carry-under (GCU), bubbles or bubbly filaments escape with the liquid flow from the liquid outlet. Clearly, these two phenomena should be avoided to the greatest extent possible in the design and operation of the GLCC. However, in most real applications, the quality of the separated fluid at one outlet must be sacrificed to satisfy the separation requirement at another outlet.

The investigation of the droplet size distributions and the flow pattern composed of the droplets and liquid film, which depend on the source of the LCO, is essential. Molina et al. (2008) and Gomez et al. (1999) developed a prediction model for the phase distribution in a GLCC by analyzing the migration route of the droplets. However, few

* Corresponding author.
E-mail address: zhaizhf@mail2.sysu.edu.cn (Z. Zhai).

https://doi.org/10.1016/j.jngse.2022.104465
Received 8 September 2021; Received in revised form 7 January 2022; Accepted 6 February 2022
Available online 8 February 2022

Fig. 1. Conventional vessel-type separator.

studies (particularly experimental investigations) on the droplet size distribution in the GLCC have been performed. By performing flow visualization under various inflow operating conditions, Hreiz et al. (2014a) observed three types of flow regimes: churn flow, annular flow, and ribbon flow. The transition of the flow patterns is mainly determined by the inlet gas and liquid flow rates. Yue et al. (2019) investigated the flow regimes and flow characteristics of an upper swirling liquid film using experimental and numerical approaches. They added a swirling flow based on the flow patterns observed by Hreiz et al. (2014a), and the corresponding flow-pattern maps were presented. They found that the surface tension and viscosity affected the flow patterns. In fact, the differential pressure at the two outlets significantly affected the droplet size distribution and flow patterns. However, in previous studies, the relationship between the differential pressure and the droplet size distribution or flow patterns was seldom considered.

With regard to the GCU, the behavioral characteristics of bubbles and bubbly filaments in the lower part of the GLCC play an important role. Sanmiguel (1998) improved a previously developed bubble trajectory model (Marti et al., 1996) by assuming a local momentum equilibrium to track a single bubble in the predicted flow field. According to observations of the flow phenomena in the GLCC, Hreiz et al. (2014a) defined four vortex flow patterns: gravity-dominated flow, bubbly vortex flow, excavated vortex flow, and deeply excavated vortex flow. They discovered that the liquid flow rate significantly affected the flow pattern in the lower part of the GLCC. The gas flow rate can increase the bubble density but has less influence on the vortex flow patterns. Hreiz et al. (2014b) performed laser Doppler velocimetry measurements and observed that the hydrodynamics of the vortex core is complex, and turbulent and laminar flows appeared alternately in the lower part of the GLCC. Most of these previous studies on bubbles and bubbly filaments have been restricted to qualitative research.

The GLCC has the advantages of a small volume, high efficiency, low cost, and large treatment capacity and has been used in field applications for partial gas–liquid separation (Hsiao et al., 2015) or multiphase meters (Wang et al., 2010). However, the GLCC has not been widely used as a conventional vessel-type gas–liquid separator, which has significant advantages with regard to reliability and management convenience (Huang et al., 2018). There are two main reasons hindering its merited expansion. First, it remains difficult to predict the complex hydrodynamic performance of GLCCs (Hreiz et al., 2014b). The design of the key parameters remains mostly empirical. The effects of the swirling flow characteristics on the separation efficiency of the GLCC have not been investigated in detail (Yang et al., 2020a). Second, the residence time of the fluid in the GLCC is short; consequently, it can be easily destabilized owing to large flow variations at the inlet (Wang et al., 2010). The conventional control strategy is based on flow-rate control (Kristoffersen et al., 2017a). However, in an actual oil field, the mixture flows are not in a steady state, and the flow rates and gas–liquid ratio always vary with time. The small volume of the GLCC makes it sensitive to these variations (Kristoffersen et al., 2017b). Multiphase metering is a global problem (Hansen et al., 2019). The measurement accuracy is low, and the cost is high. It is particularly difficult to measure the gas–liquid flow rates for subsea separators. Consequently, it is difficult to ensure that the tube separators achieve good separation performance by regulating the flow rates at both outlets (Yang and Xu, 2017).

In this work, a pressure control scheme is proposed to enable the GLCC to realize fast and stable gas–liquid separation. The droplet size distributions at the inlet and in the GLCC body were measured using a Malvern RTSizer. The distribution of bubbles and bubbly filaments was measured quantitatively via electrical resistance tomography (ERT). The effect of dimensionless pressure on the droplet size distribution was investigated and physically explained in combination with a previously proposed droplet migration model. The bubble migration in the swirling flow field under different dimensionless pressures were characterized using the ERT data matrix.

2. Experimental setup

2.1. Working fluids

In this study, a mixture of air and tap water was applied for separation. At 20 °C, the density of air was 1.205 kg/m^3, with a viscosity of 0.018 mPa s, and the density of tap water was 998.0 kg/m^3, with a viscosity of 1.0 mPa s. The produced liquid in oil field is oli-gas-water mixture. The water content of the produced liquid increases over exploitation time. In mature oil wells, the water content always exceeds values of 90%. The physical characteristics of the oil-water mixture with high water content is almost the same with that of pure water.

The cyclone performance coefficient is a function of dimensionless parameters (Burkholz, 1989)

$$\Psi = Stk \cdot Re^{1/3} \cdot \left(\frac{Eu}{2}\right)^{2/3} \tag{1}$$

where *Stk*, Re and *Eu* are the Stokes number, Reynolds number and Euler number, respectively

$$Stk = \frac{\rho_l d^2 V_g}{\mu_g D};\ Re = \frac{\rho_g V_g D}{\mu_g};\ Eu = \frac{2\Delta P}{\rho_g V_g^2} \tag{2}$$

where d is the droplet diameter, μ_g is the dynamic viscosity of gas, ρ_g is the density of gas, ρ_l is the density of liquid, V_g is the velocity of gas, ΔP is the pressure drop from the separator inlet to outlet, D is the cyclone body diameter.

Hoffmann and Stein (2008) give a more accurate expression for Stokes number, as follows:

$$Stk_H = \frac{\Delta\rho d^2 V_g}{18\mu_g D} \tag{3}$$

where $\Delta\rho$ is the difference between liquid and gas densities.

The separation performance is also effected by the droplet breakup that is related to the Weber number

$$We = \frac{\rho_g V_g^2 D}{\sigma} \tag{4}$$

where σ is the surface tension.

The Ψ parameter mainly describes the similarity of the separation process of particles from the gas-liquid mixture (Mikheev et al., 2018). Taking the produced liquid in one Nanhai oilfield of China as an example, the comparison of test liquid and produced liquid is shown in Table 1. Due to slight difference of flow parameters, it is reasonable to

Table 1
Flow parameters of test liquid and produced liquid.

Parameter	Unit	Test liquid	Produced liquid
ρ_g	kg/m^3	1.205	1.024
ρ_l	kg/m^3	998	993
μ_g	10^{-5} Pa s	1.8	1.54
μ_l	10^{-5} Pa s	100	145
V_g	m/s	16	16
D	m	0.05	0.05
d	μm	30	30
ΔP	kPa	5	5
σ	N/m	0.072	0.072
Stk_H		0.88	1.03
Re	10^5	5.36	5.32
We		214	182
Ψ	10^2	2.14	2.78

replace the oil-water-gas mixture with water-air mixure to conduct experiments for convenience and safety.

2.2. Flow loop

A multiphase circulation system was specially designed for this study. Figs. 2 and 3 show a flowchart and photographs of the experiment, respectively. The inlet water flow rate to the mixer was controlled by regulating the pump speed, and a Coriolis mass flowmeter was used to measure the flow rate. The inlet air flow rate was controlled using a butterfly valve and then measured using a thermal gas mass flowmeter. Subsequently, air and water were mixed in a pressure-swirl nozzle, as shown in Fig. 3b (detailed configuration refers to Mao et al. (2020)), and atomized droplets were formed. The size distributions of the atomized droplets at the inlet were measured online using a droplet size analyzer (Malvern RTSizer).

The air–water mixture flowed into the GLCC. Numerous droplets were dragged toward the pipe wall under the centrifugal effect and coalesced into the liquid film. The liquid film could fall because of gravity or move up owing to the drag of the high-velocity gas flow. The upward-moving liquid film was removed using two annular film extractors (AFEs), as shown in Fig. 3c. The size distributions of the remaining droplets, which were located 345 and 660 mm below the top, were measured online using the Malvern RTSizer. The sampling outlets located 345 and 660 mm below the top were marked as up sampling outlet and down sampling outlet, respectively. The water emerging at the gas outlet was collected and measured using a volumetric measurement technique. In the lower part of the GLCC, the droplets gathered to become a continuous phase, and dense bubbles appeared under the effect of turbulent shear. Large bubbles quickly moved back to the free interface owing to buoyancy. Small bubbles were carried over with the liquid stream and migrated to the vortex center to generate a bubbly filament. The local void fraction was measured using an ERT 3000 instrument, which has proven to be reliable for extracting flow information from various multiphase flows (Jia et al., 2010, 2015; Singh et al., 2017). It contained two electrodes with circular shapes, which were placed 370 and 420 mm above the liquid outlet. The gas volume fraction of the mixture at the liquid outlet was small and was measured using a Coriolis mass flowmeter. The pressures at the inlet and outlet were controlled using diaphragm valves and metered by pressure transmitters.

2.3. Measurement methods of droplet size distribution

Malvern RTSizer was used to measure the droplet size distribution at the inlet and both sampling outlets. The measurement principle was based on the diffraction of a parallel beam through a dispersed particulate sample. The interference fringes formed by the diffraction were detected by a group of photosensitive rings and the energy spectrum of the interference fringes could be measured. This data is then analyzed to calculate the size of the particles that created the scattering pattern. Hirleman et al. (1984) discovered that, due to a combination of detector calibration errors and nonideal lens effects, variations of about 15% in the instrument response with three standard receiving lenses. Kusters et al. (1991) indicated that serious errors could occur when a Malvern 2600 instrument using a scattering matrix corresponding to a refractive-index ratio of about 1.2 is used to size systems with refractive-indexratios near 1. In this study, the refractive index ratio of the Malvern RTsizer was set according to a test medium, and a background measurement was performed before each test. The average deviation is less than 10%.

2.4. GLCC configuration

All tubes were fabricated using plexiglass to allow visual observation. The cyclone was 1980 mm in height and 50 mm in diameter. As shown in Fig. 4, the inclined inlet pipe had a 25-mm inner diameter without restriction and an inclination angle of 27°, as suggested by Kouba et al. (1995). The inlet pipe was tangent to the GLCC body, and located 1070 mm below the top of the GLCC body. The gas outlet—a

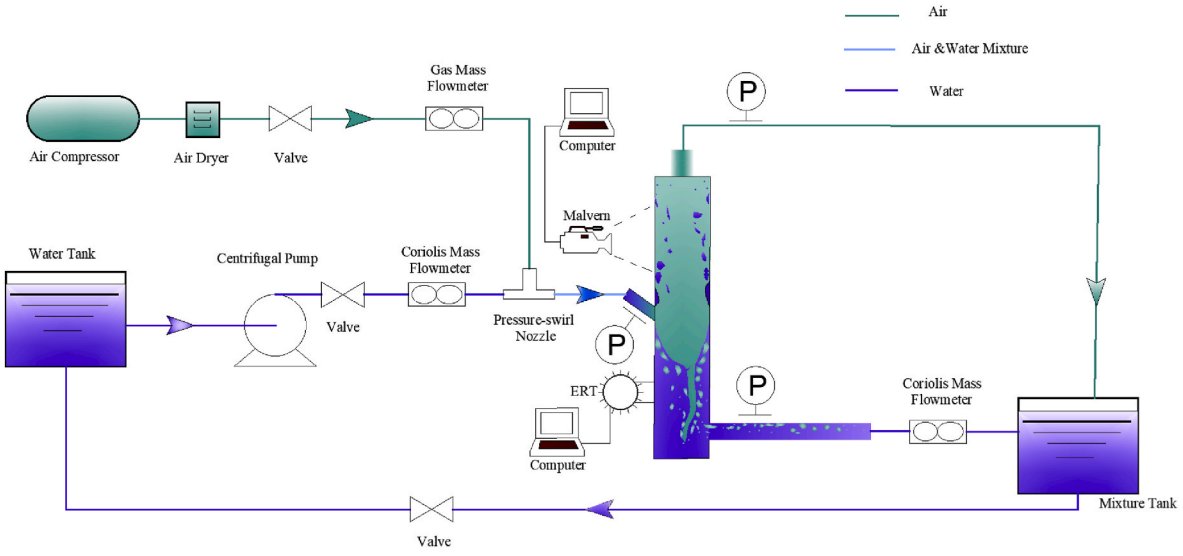

Fig. 2. Schematic of the experiment loop.

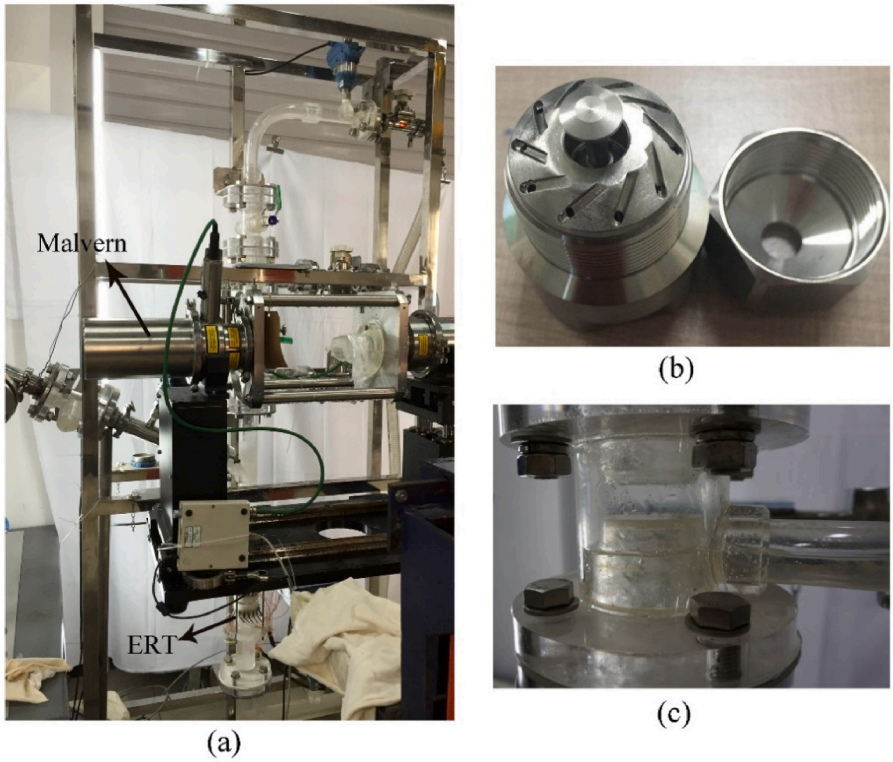

Fig. 3. Experimental photographs: (a) experimental setup; (b) pressure-swirl nozzle; (c) AFE.

25-mm-inner diameter pipe—was at the top of the GLCC. The liquid outlet was a 50-mm-inner diameter pipe 780 mm below the inlet plane.

2.5. Experimental conditions

The inlet conditions and operational envelope for the LCO are presented in Fig. 5. The GLCC operational envelope refers to the combination of gas and liquid flow rates corresponding to the onset of LCO when the liquid level was below the inlet and above the liquid outlet. The inlet conditions at the right of the LCO curve refer to the operating conditions that produced the LCO. Therefore, the optimal operating region for gas–liquid separation lies to the left of the data points. As shown in Fig. 5, the operational envelope depended mainly on the gas superficial velocity. Five superficial liquid velocities (0.085–0.555 m/s) and eleven superficial gas velocities (12–64 m/s) were applied in the experimental test, covering a wide range of Reynolds number between 9.97×10^4 and 5.97×10^5. For each of the resulting 55 combinations of experimental conditions, the droplet size distribution, void fraction distribution, flow rate, density, and gauge pressure were measured online. In each step of the measurement process, the data were measured several times after the flow became stable, to minimize the measurement error.

3. Results and discussion

3.1. Pressure control strategy

The liquid level is an important parameter for gas–liquid separation performance. In a previous study (Yang et al., 2020a), when the liquid level was below the inlet and above the liquid outlet, almost all the liquid flowed out through the liquid outlet. Simultaneously, the liquid level provided a barrier against downward gas flow. Thus, almost the entire volume of gas flowed directly above the inlet of the GLCC. A gas–liquid mixture can achieve good separation in this situation. When the liquid level was above the inlet, large droplets were formed under the shear action of the high-speed gas flow on the liquid phase. These droplets moved upward with the high-speed gas flow, which caused a large amount of liquid to flow out from the gas outlet. This situation should be avoided during gas–liquid separation. Therefore, the liquid level should remain below the inlet and above the liquid outlet during the normal operation of the GLCC.

In the experimental tests, the pressure at one outlet remained untouched, while the pressure at the other outlet was slowly regulated to obtain flow patameters under different differential pressures. Fig. 6 shows the liquid levels measured from GLCC bottom for different differential pressures between the two outlets. As the differential pressure between the gas and liquid outlets increased, the liquid level tended to increase. When the liquid level remained below the inlet and above the liquid outlet, the liquid level and the liquid outlet section approximately satisfied the extended Bernoulli equation, as expressed by Eq. (5). With an increase in the differential pressure, namely higher pressure at the gas outlet or lower pressure at the liquid outlet, the liquid volume at the liquid outlet did not change significantly, indicating that the velocities of the two sections were approximately equal. Therefore, an increase in the differential pressure led to a gradual increase in the liquid level. When the liquid level rose above the inlet, it became easier for the liquid to flow away from the liquid outlet, resulting in a sharp rise in the liquid level. Therefore, in practical applications, the liquid level in the GLCC can be remained below the inlet and above the liquid outlet by setting a reasonable differential pressure based on Eq. (6) to achieve a good separation performance.

Extended Bernoulli equation can be expressed as follows:

$$z_1 + \frac{p_1}{\rho g} + \frac{U_1^2}{2g} = z_2 + \frac{p_2}{\rho g} + \frac{U_2^2}{2g} \tag{5}$$

where z_1 represents the height of liquid outlet; z_2, the height of liquid level; U_1, the liquid velocity at the liqiud outlet; U_2, the liquid velocity at the liqiud level; p_1-p_2 is approximately equal to the differential pressure between the two outlets.

It can be derived from $U_1 \approx U_2$ as follows:

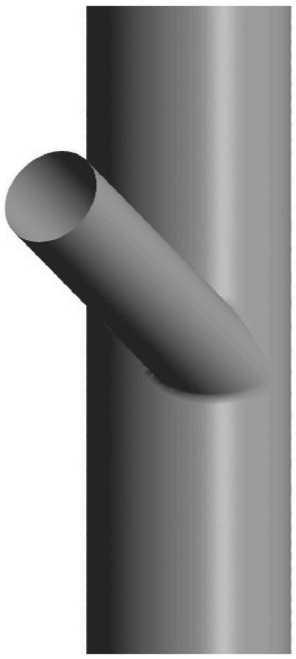

Fig. 4. Inlet configuration.

$$z_2 - z_1 = \frac{1}{\rho g}(p_1 - p_2) \tag{6}$$

The separation efficiency of the GLCC is expressed as the ratio of the amount of LCO to the inlet liquid flow rate (Molina et al., 2008), as follows:

$$\eta = 1 - \frac{Q_{l3}}{Q_{l1}}, \tag{7}$$

where Q_{l1} represents the inlet liquid flow rate, and Q_{l3} represents the flow rate of the liquid entrained in the gas stream.

The dimensionless pressure is defined as the ratio of the pressure drop between the inlet and gas outlet to the pressure at the liquid outlet, as follows:

$$\overline{P} = \frac{P_1 - P_3}{P_2}, \tag{8}$$

where the subscripts 1, 2, and 3 refer to the inlet, liquid outlet, and gas outlet, respectively.

Considering the system pressure, Yang et al. (Yang and Xu, 2017) proposed the concept of a dimensionless pressure for a gas–liquid Y-junction separator, as defined in Eq. (8). According to an analysis of the experimental data, it was concluded that the dimensionless pressure can reflect the physical laws more accurately than the differential pressure. Similarly, in the present study, the dimensionless pressure was used to investigate the separation characteristics in the GLCC. Besides the pressure drop, the system pressure also has a significant influence on the gas-liquid separation because the gas is compressible. In Eq. (8), the pressure drop from the inlet to the gas outlet represents the system pressure drop, and the pressure at the liquid outlet represents the system pressure. Fig. 7 shows the effect of the dimensionless pressure on the separation efficiency. The separation efficiency increased as the dimensionless pressure decreased. This phenomenon is directly related to the variation in flow regimes with changes in the dimensionless pressure, which will be discussed in detail in Section 3.4. For low liquid superficial velocities (0.192 and 0.283 m/s), the atomization effect of the inlet nozzle was good. These atomization droplets were easy to be transported by the gas stream. Higher liquid superficial velocity

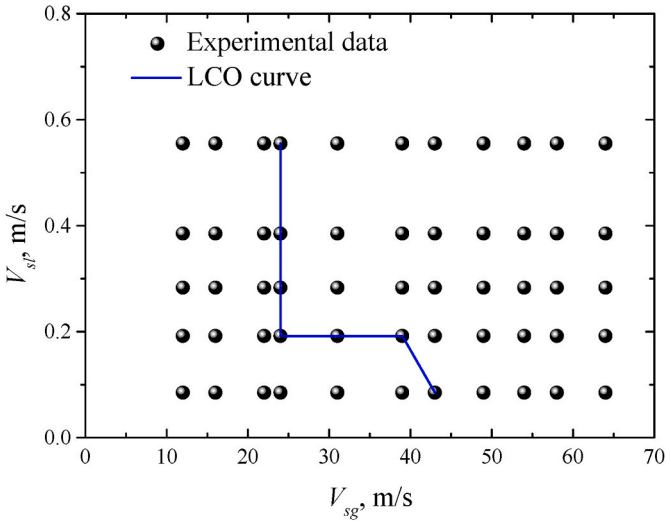

Fig. 5. Inlet conditions and operational envelope for LCO.

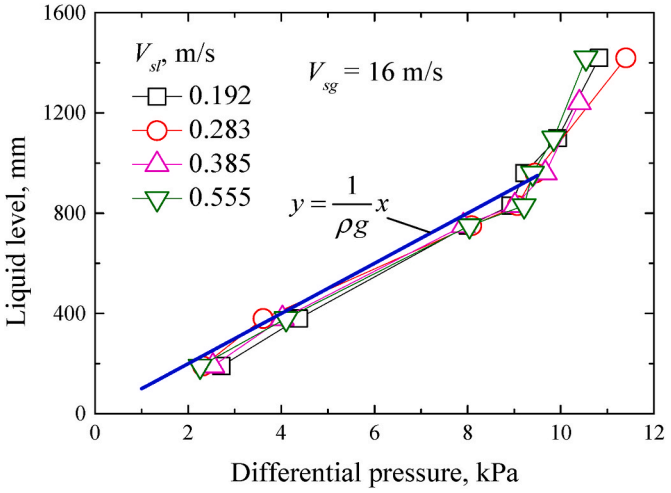

Fig. 6. Liquid levels measured from GLCC bottom for different differential pressures between two outlets.

produced more droplets. To achieve the same separation efficiency, it was necessary for the situation of higher liquid superficial velocity to keep a smaller dimensionless pressure, namely higher backpressure at the gas outlet or lower backpressure at the liquid outlet. As the liquid superficial velocity increased further, the atomization effect of the inlet nozzle became worse. The proportion of continuous phase and large droplets to the total inlet liquid volume increased. It became more difficult for continuous phase and large droplets to be transported upward by the gas streams. In this case, a larger dimensionless pressure was enough for the situation of higher liquid superficial velocity to achieve the same separation efficiency.

3.2. Droplet size distributions

The separation performance of the GLCC was significantly influenced by the flow-field characteristics at the inlet. Therefore, the droplet distribution at the inlet was measured. Figs. 8 and 9 show the effects of the liquid and gas superficial velocities on the characteristic sizes of the droplet size distribution. d_x refers to the value corresponding to the x percentage finer size. d_{32} represents the Sauter mean diameter, which is used to monitor the small droplets, and d_{43} represents the De Brouckere mean diameter, which is used to monitor the large droplets. As the liquid

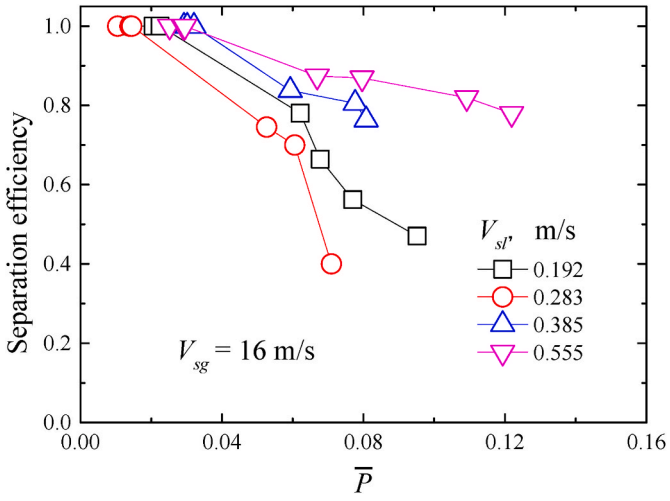

Fig. 7. Effect of the dimensionless pressure on the separation efficiency.

superficial velocity increased, d_{10} increased, while d_{50} and d_{90} remained stable. This implies that the liquid superficial velocity mainly affected the small-droplet distribution rather than the medium- and large-droplet distributions. However, the increasing gas superficial velocity led to a decrease in the droplet size distribution as a whole. This influence was less pronounced for higher superficial liquid velocities. These behaviors were due to the formation mechanism of the droplets. In the pressure-swirl nozzle, the liquid was forced to flow along a helical path and disintegrated into a cluster of thin sheets. The surface instability and shear action were induced by the slip velocity between the gas and liquid phases. The surface waves propagated from the atomizer orifices. Owing to the expansion, the wave magnitude increased, and the thickness of the thin sheets decreased. Finally, the wave disintegrated into ligaments and fine droplets. In this process, the gas kinetic energy was used to overcome the surface tension, viscous force, and other resistances. A relatively high gas superficial velocity can promote the shear effect and flow instability, resulting in droplets with small diameters. However, the number of droplets increased as the liquid superficial velocity increased, which in turn increased the probability of drop coalescence and the energy consumption during the atomization process. Meanwhile, small droplets tended to coalesce, while large droplets remained steady owing to the limited carrying capacity of the gas. Thus, at a given gas superficial velocity, the liquid superficial velocity mainly affected the

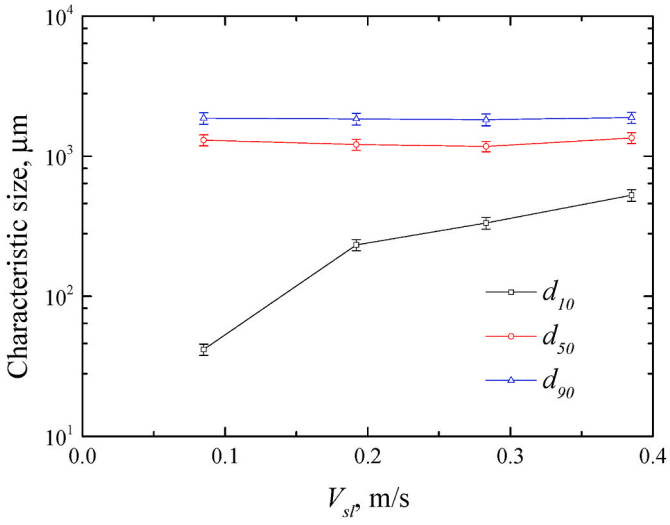

Fig. 8. Measured droplet size distribution at the inlet for different liquid superficial velocities under V_{sg} = 64 m/s.

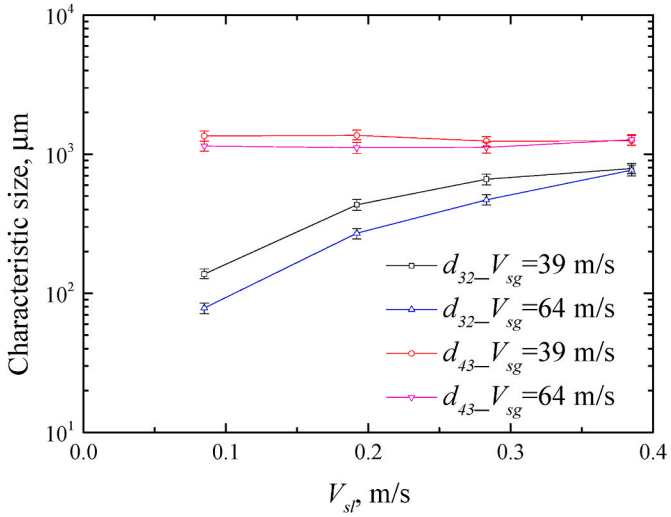

Fig. 9. Effect of the gas superficial velocity on the measured droplet size distribution at the inlet.

distribution of the small droplets rather than the larger droplets. The influence of the gas superficial velocity on the atomization became less obvious when the liquid superficial velocity reached a certain level.

When the inlet liquid superficial velocity was set at 0.192 m/s and the inlet gas superficial velocity changed from 31 to 64 m/s, the droplet size distributions at the inlet, down sampling outlet and up sampling outlet were carefully recorded. The characteristic sizes are shown in Fig. 10. All the characteristic sizes decreased significantly after separation at the inlet. However, the characteristic sizes changed little between the two sampling outlets in the upper part of the GLCC. According to the research results of Zhang and Xu (2016), the decline of the Sauter mean diameter (d_{32}) suggested that the turbulent dissipation energy increased, which implied a more turbulent flow. According to the variation of d_{32}, the degree of disorder of the gas–liquid flow after it entered the GLCC body could be determined. The swirling flow fields between the two sampling outlets had almost the same degree of disorder.

3.3. *Effect of dimensionless pressure on droplet size distribution*

The experimental results of Wang (2000) and Yang et al. (2020a) indicated that when the liquid level was below the inlet and above the liquid outlet, it had little effect on the liquid removal efficiency. However, when the liquid level rose above the inlet level, the flow became very disordered at the inlet. The gas stream carried large amounts of splashing droplets toward the gas outlet. Because of the flow instability, this situation often occurs in practical applications—particularly in subsea separation. The liquid level is related to the dimensionless pressure, as described in Section 3.1. Therefore, it is necessary to investigate the effect of the dimensionless pressure on the droplet size distribution when the liquid level is above the inlet level.

Fig. 11 shows the droplet size distributions for different dimensionless pressures, and Table 2 presents the corresponding characteristic sizes, where the liquid level is above the inlet. According to experimental data, despite inlet superficial velocities, the effects of dimensionless pressure on droplet size distribution were similar. As shown, the droplet size distribution of the down sampling at a high dimensionless pressure was larger overall than that at a low dimensionless pressure. A high dimensionless pressure implies that the backpressure at the gas outlet decreases or the backpressure at the liquid outlet increases, which makes the gas flow containing droplets more likely to flow out through the gas outlet. More droplets moved upward; thus, the probability of collisions among droplets increased, leading to an increase in the droplet size distribution as a whole. However, for upsampling, the droplet size

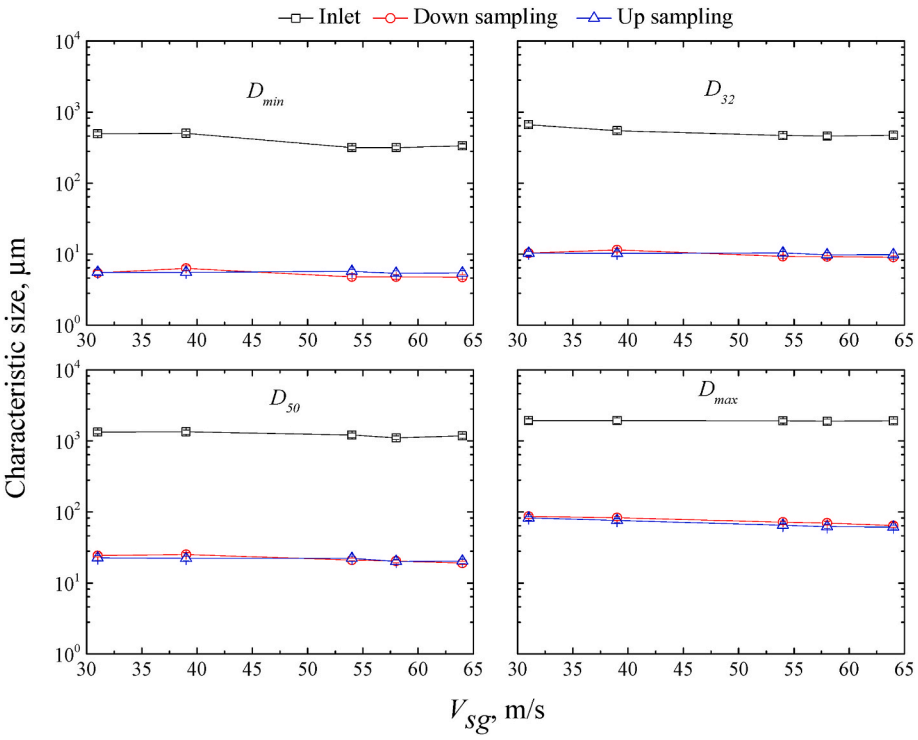

Fig. 10. Characteristic sizes at the inlet, down sampling and up sampling under $V_{sl} = 0.192$ m/s.

distributions at different dimensionless pressures were almost identical. Although the droplets were more likely to coalesce into larger droplets at a high dimensionless pressure, these coalesced droplets could migrate to the wall over a shorter distance. This phenomenon can be verified by the droplet migration model (Yang et al., 2020a), as expressed by Eq. (9). This mechanism model was developed according to the force analysis of

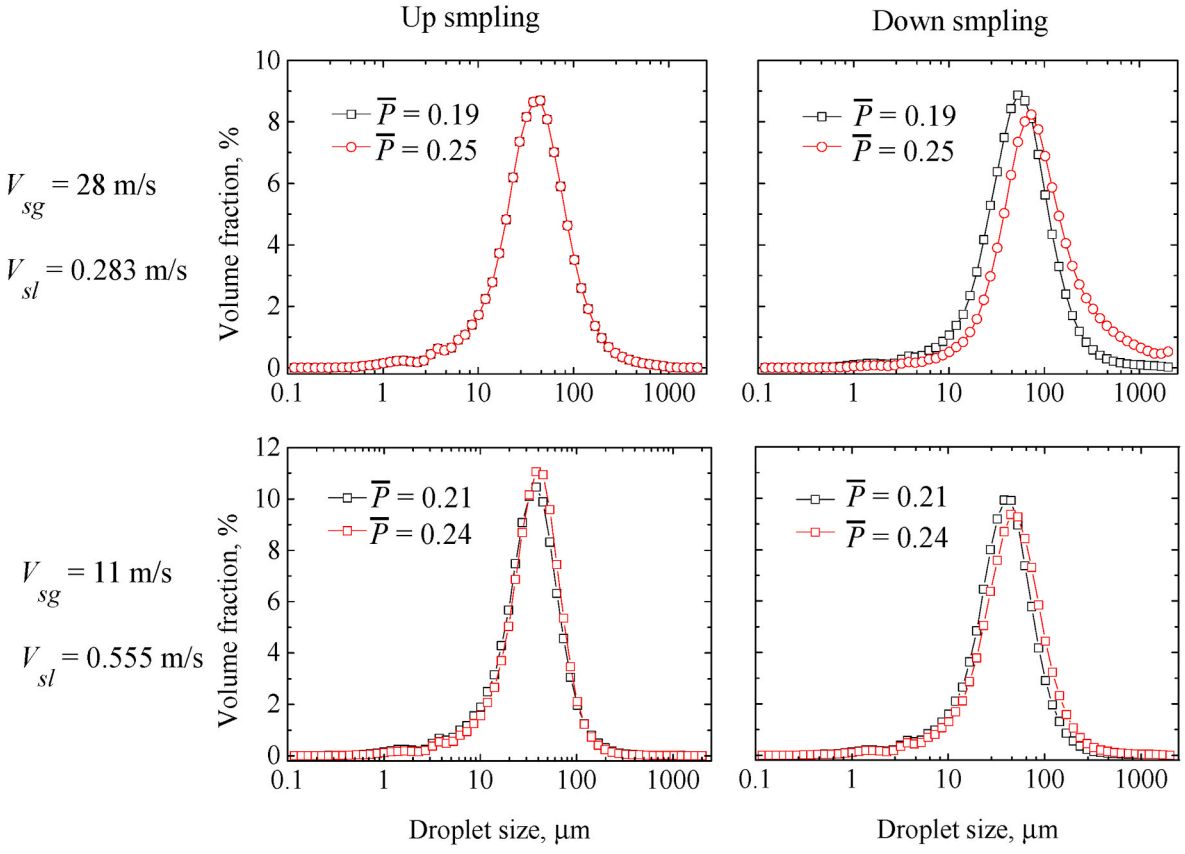

Fig. 11. Droplet size distributions for different dimensionless pressures.

the droplet and swirling hydrodynamics in the GLCC. The predicted migration paths of the droplets with different sizes for the structure used in this study are shown in Fig. 12. The migration distance was not linear with respect to the droplet diameter. As the droplet diameter decreased, equal intervals of the droplet diameter corresponded to increasing amounts of axial space. Therefore, it was diffucult to capture very small droplets by increasing the length of the GLCC. This indicated that increasing the length of the GLCC excessively made little benefits in the separation performance. The sampling outlet was farther from the inlet than the down sampling outlet thus, these droplets had more time to migrate to the wall or flow away from the two AFEs before reaching the up sampling outlet. Therefore, the dimensionless pressure had little influence on the droplet size distributions of the up sampling.

The trajectory of the droplet can be expressed as follows:

$$\Delta z_d = \int \frac{v_{SG} - v_{dz}(r)}{v_{dr}(r)} dr, \tag{9}$$

where v_{dz} represents the axial slip velocity, v_{dr} represents the radial slip velocity, and v_{SG} represents the gas velocity in the body of the GLCC.

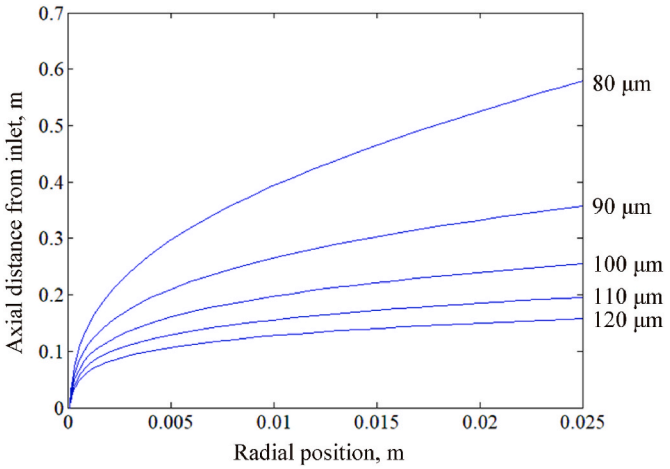

Fig. 12. Predicted migration paths of droplets with different sizes.

3.4. Effects of dimensionless pressure on flow regimes

Fig. 13 shows the variation in the flow regimes in the elbow pipe with a reduction in the dimensionless pressure. For the case shown in the figure, the gas and liquid superficial velocities were 16 and 0.283 m/s, respectively. According to the experimental observations, the other cases had similar variation laws for the flow regimes. A thick annular liquid film can occur at a high dimensionless pressure, as shown in Fig. 13a (see Video "Annular flow"). This is because a large amount of liquid and almost all the gas directly enters the upper part of the GLCC when the dimensionless pressure is high. At a high dimensionless pressure, the backpressure at the gas outlet was low or the backpressure at the liquid outlet was high, resulting in a low resistance in the GLCC. Therefore, the gas had a high upward velocity, where the gas-liquid interface became wavy due to the well-know Kelvin-Helmholtz instability. The surface tension force had a stabilizing effect, whereas the drag force caused by the relative velocity between the phases destabilized the liquid film, which was the same with conventional vertical gas-liquid flow. A portion of the wavy liquid film along the pipe wall can break into several droplets and be entrained into the gas flow in a number of different ways (Ishii and Grolmes, 1975). Negative impact of these processes on separation efficiency increased progressively with the growing gas dynamic head inside the separator. However, different from conventional vertical gas-liquid flow, the washing of the liquid film took place under conditions of the tangential component of the gas velocity in the separator (Saushin et al., 2019). In addition, strong swirling flow can push back the entrained droplets towards the wall. Under the strong carrying capacity, the high-speed gas flow dragged a large amount of liquid upward in the form of a thick annular film.

With a reduction in the dimensionless pressure, the backpressure at the gas outlet increased or the backpressure at the liquid outlet decreased, leading to an increased resistance in the GLCC. Both the upward velocity of the gas and the amount of entrained liquid decreased. A higher flow resistance caused the swirl intensity to decay more rapidly; thus, the swirl intensity in the elbow pipe was significantly reduced compared with that at the inlet. The weak centrifugal force was not adequate to allow the droplets to quickly migrate to the wall and keep the liquid film steady. Therefore, the gas–liquid flow became turbulent and chaotic. The gas stream always tried to carry the unsteady liquid film upward; thus, unsteady vertical flow oscillations occurred in the vertical section of the elbow pipe. This flow regime is called churn flow, which is similar with "churn flow" in conventional vertical gas-liquid flow. However, under the same gas and liquid velocities, the amount of droplets in the GLCC is less than that in conventional vertical gas-liquid flow because of the centrifugal effect. In addition, due to the existence of two outlets, a portion of the liquid film and droplets in the upper part of the GLCC fell back to the lower part of the GLCC. When the gas–liquid mixture arrived in the horizontal section of the elbow pipe, the flow regime transitioned from churn flow to stratified flow, as shown in Fig. 13b (see Video "Churn flow to stratified flow").

As the dimensionless pressure increased further, the high flow resistance significantly slowed the gas–liquid flow. The carrying capacity of the low-flow rate gas stream decreased significantly, and the residence time of the liquid in the upper part of the GLCC increased so that the liquid dropped back more easily during upward motion under the effect of gravity. Only small amounts of droplets clinging to the wall reached the elbow pipe, as shown in Fig. 13c (see Video "Falling droplets"). This flow regime looks like the conventional "mist flow", namely that all the liquid becomes entrained as droplets in the gas flow. Mist flow occurs at very high gas flow rates and very high flow quality. This conditions causes that liquid film flowing on the pipe wall is thinned by the shear of the gas core on the interface until it becomes unstable and is destroyed. The droplets in the mist flow has an upward velocity, which is different from the flow regime of "falling droplets" in the GLCC.

When the dimensionless pressure increased to a critical range where it contributed to a separation efficiency of almost 100% (Fig. 7), no liquid emerged in the elbow pipe, and pure gas flowed out from the gas

Table 2
Characteristic size.

V_{sg} (m/s)	V_{sl} (m/s)	$\overline{P}$	Sampling	d_{10} (μm)	d_{32} (μm)	d_{43} (μm)	d_{50} (μm)	d_{90} (μm)
28	0.283	0.19	Up	11.37	18.90	54.74	37.44	108.44
			Down	15.57	24.96	69.58	48.62	131.01
28	0.283	0.25	Up	10.95	18.16	50.96	36.06	98.78
			Down	24.45	40.03	146.91	72.50	310.52
11	0.555	0.21	Up	10.24	16.48	38.23	31.25	69.66
			Down	11.69	18.69	45.61	35.13	82.92
11	0.555	0.24	Up	11.99	18.73	39.62	33.81	70.66
			Down	13.44	21.42	55.67	41.70	104.37

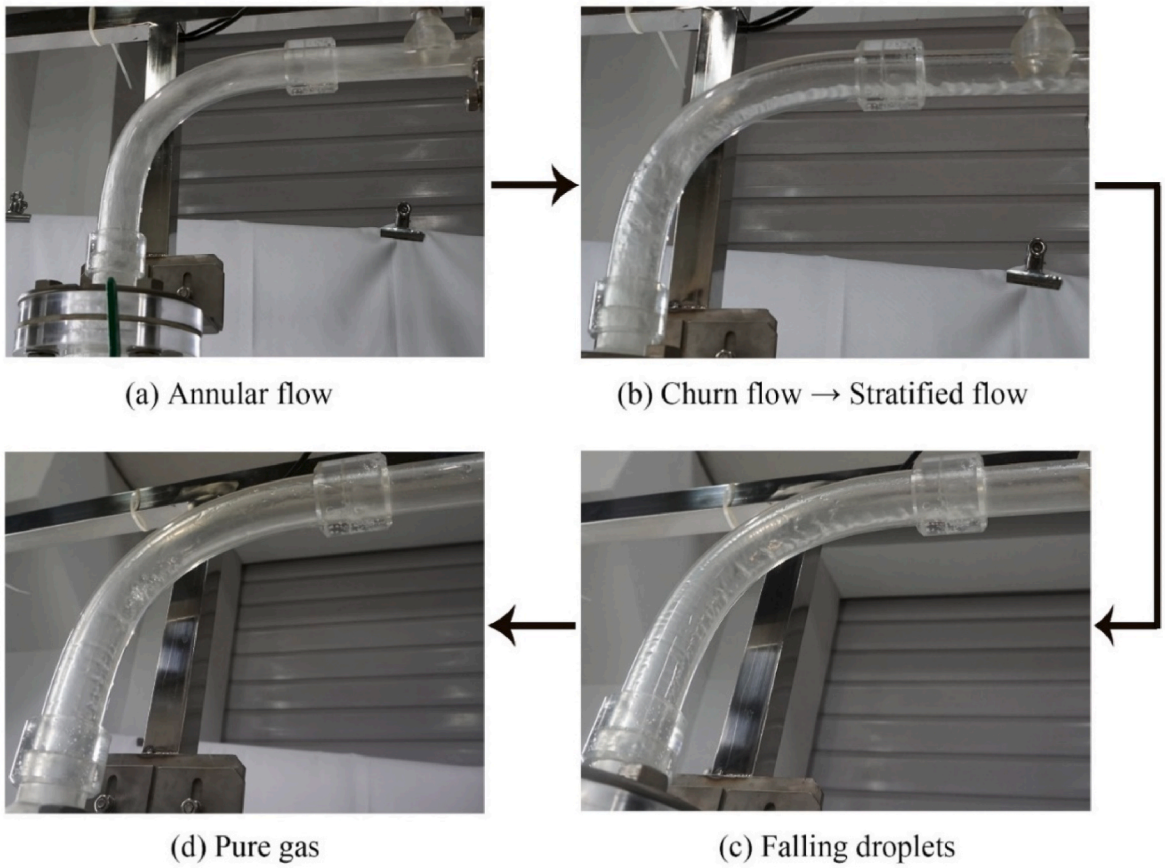

Fig. 13. Variation of flow regimes with a reduction in the dimensionless pressure.

outlet, as shown in Fig. 13d (see Video "Pure gas"). However, when the dimensionless pressure increased to a certain extent, the gas fraction at the liquid outlet increased rapidly. This is because owing to the reduction in the liquid level, many bubbles reached the liquid outlet and only migrated a short distance.

3.5. Effect of dimensionless pressure on bubble concentration in lower part of GLCC

In the lower part of the GLCC, the bubbles became the dispersed phase. The effect of the dimensionless pressure on the bubble concentration was characterized using the ERT data matrix. Fig. 14 shows the cross-sectional gas volume fraction distributions for several dimensionless pressures. In the ERT images, the red region represents a high gas-phase concentration, and the blue region represents a low gas-phase concentration. Fig. 15 presents the cross-sectional volume fraction at the horizontal centerline for several dimensionless pressures. At a low dimensionless pressure of 0.058, the bubbles were dispersed throughout the cross section, indicating that the short distance was not sufficient for most bubbles to migrate to the pipe center. Better convergence of the bubbly filament was observed at a dimensionless pressure of 0.068. This is attributed to the higher liquid level, which provided a longer distance for the phase-transfer process in the radial direction. As the dimensionless pressure increased further, the gas-core region gradually shrank, and the local void fraction decreased significantly, owing to the emergence of a flow-reversal region in the central zone of the pipe (Hreiz et al., 2014b; Yang et al., 2020b). When the dimensionless pressure increased to 0.097, almost all the bubbles had reached the pipe center and reversed back to the free surface; thus, only small bubbles remained in the bubbly filament. Therefore, the gas volume fraction decreased as the dimensionless pressure increased, which was confirmed by integrating the cross-sectional volume fraction, as shown in Fig. 16. However, as shown in Fig. 7, with an increase in the dimensionless pressure, the separation efficiency decreased, namely that the amount of LCO increased. It can be determined that there is an optimum value for the dimensionless pressure that can balance acceptable GCU with minimum LCO. In general, the optimum dimensionless pressure value locates at the turning point in Fig. 7 where separation efficiency begins to decrease.

4. Conclusion

An experimental investigation of gas–liquid flow splitting in the GLCC was conducted. Five superficial liquid velocities (0.085–0.555 m/s) and eleven superficial gas velocities (12–64 m/s) were applied in the experimental test, covering a wide range of Reynolds number between 9.97×10^4 and 5.97×10^5. For each of the resulting 55 combinations of experimental conditions, the pressures at two outlets were adjusted to investigate the flow parameters under different working conditions. The following conclusions were drawn.

When the liquid level was below the inlet and above the liquid outlet, the liquid level and the liquid outlet section approximately satisfied the extended Bernoulli equation. The separation efficiency increased as the dimensionless pressure decreased.

A Malvern RTSizer was used to measure droplet size distributions. The experimental results indicated that increasing the gas superficial velocity reduced the droplet size distribution at the inlet overall, because of the shear effect and flow instability. However, increasing the liquid superficial velocity only increased the distribution of small droplets at the inlet, owing to the limited carrying capacity of the gas. All the characteristic sizes decreased significantly after separation at the inlet.

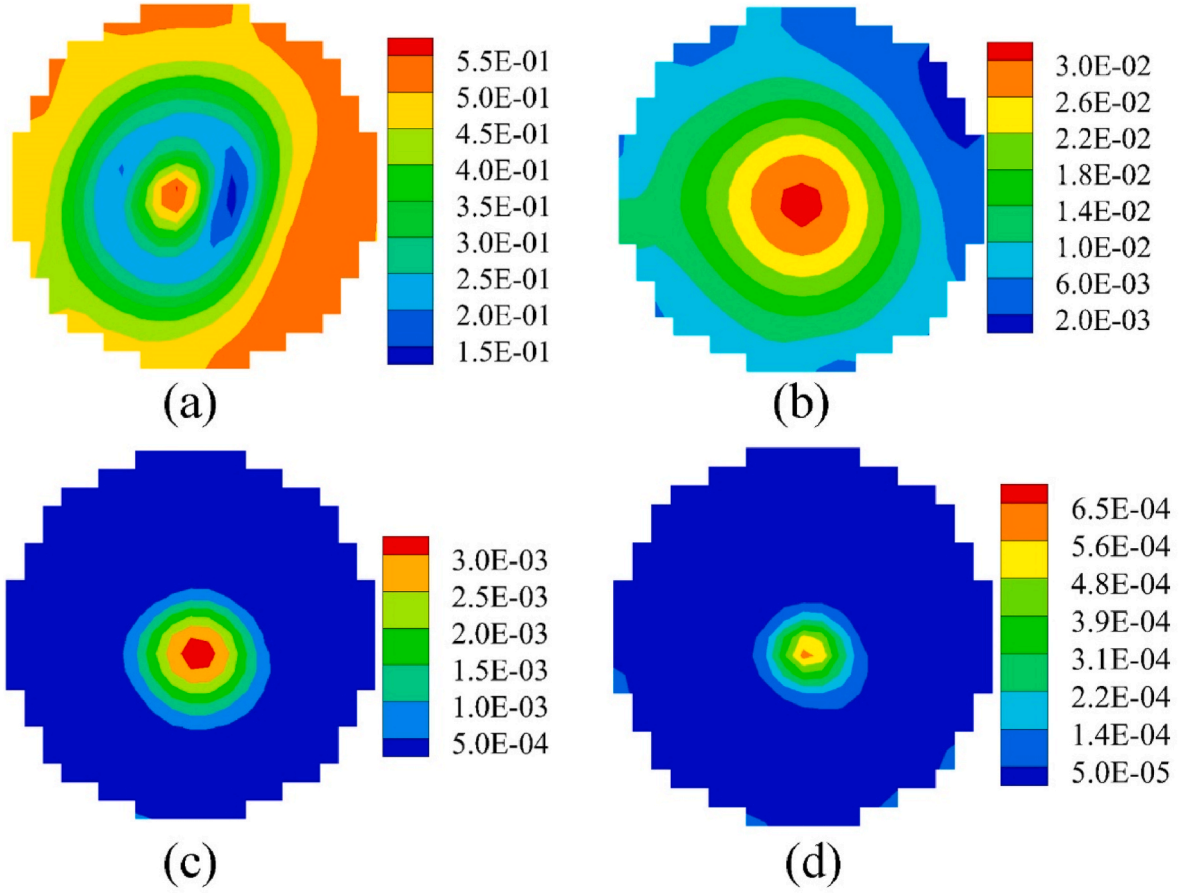

Fig. 14. Cross-sectional gas volume fraction distributions for different dimensionless pressures: (a) 0.058; (b) 0.068; (c) 0.083; (d) 0.097.

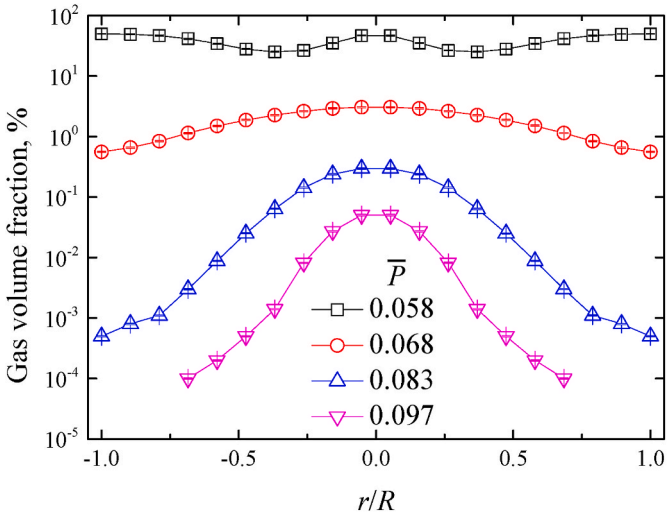

Fig. 15. Cross-sectional volume fractions at the location of horizontal centerline under different dimensionless pressures.

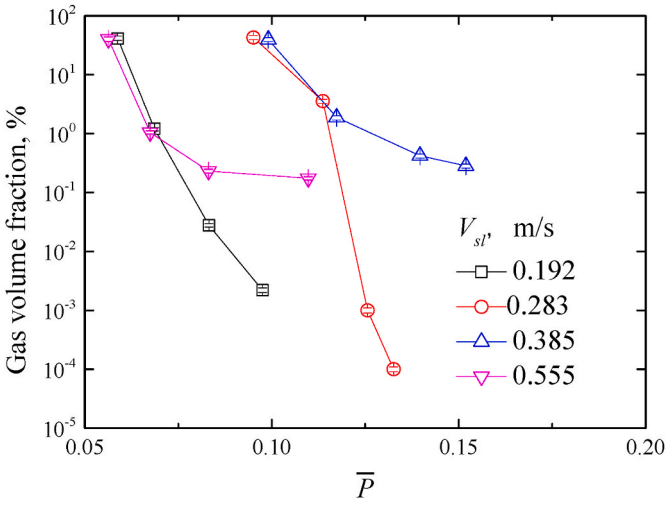

Fig. 16. Effect of the dimensionless pressure on the volume fraction of the ERT measurement section.

The droplet size distribution of the down sampling at a high dimensionless pressure was larger than that at a low dimensionless pressure, which can be explained by the droplet migration model. The dimensionless pressure had little effect on the droplet size distribution of the up sampling.

Four types of flow regimes were experimentally observed as the dimensionless pressure decreased: annular flow, churn flow-stratified flow, falling droplets, and pure gas.

The effect of the dimensionless pressure on the bubble concentration in the lower part of the GLCC was investigated via ERT measurements. The bubbly filament achieved better convergence at a higher dimensionless pressure. The void fraction decreased as the dimensionless pressure increased owing to the emergence of a flow-reversal region in the bubbly filament.

Credit author statement

Lele Yang: Writing – original draft, Writing – review & editing, Conceptualization, Methodology. Lian Luo: Writing – review & editing, Validation. Jing Wang: Investigation, Validation. Jiangyu Xu: Resources. Zhenfeng Zhai: Formal analysis Resources, Investigation.

Declaration of competing interest

The authors declare that they have no known competing financial interests or personal relationships that could have appeared to influence the work reported in this paper.

Acknowledgements

This work was financially supported by the National Key Research and Development Program of China (No. 2019YFC0312400) and the Guangdong Basic and Applied Basic Research Foundation (No. 2020A1515110155).

Appendix A. Supplementary data

Supplementary data to this article can be found online at https://doi.org/10.1016/j.jngse.2022.104465.

References

Burkholz, A., 1989. Droplet Separation. VCH.
Cai, B., Wang, J., Sun, L., Zhang, N., Yan, C., 2014. Experimental study and numerical optimization on a vane-type separator for bubble separation in TMSR. Prog. Nucl. Energy 74, 1–13.
Chen, J., Jiang, W., Han, C., Liu, Y., 2021. Numerical study on the influence of supersonic nozzle structure on the swirling condensation characteristics of CO2. J. Nat. Gas Sci. Eng. 88, 103753.
Dalane, K., Dai, Z., Mogseth, G., Hillestad, M., Deng, L., 2017. Potential applications of membrane separation for subsea natural gas processing: a review. J. Nat. Gas Sci. Eng. 39, 101–117.
Gomez, L., Mohan, R., Shoham, O., Marrelli, J., Kouba, G., 1999. Aspect Ratio Modeling and Design Procedure for GLCC Compact Separators.
Hansen, L.S., Pedersen, S., Durdevic, P., 2019. Multi-phase flow metering in offshore oil and gas transportation pipelines: trends and perspectives. Sensors 19, 2184.
Hirleman, E.D., Oechsle, V., Chigier, N.A., 1984. Response characteristics of laser diffraction particle size analyzers: optical sample volume extent and lens effects. Opt. Eng. 23, 235610.
Hoffmann, A.C., Stein, L.E., 2008. Gas Cyclones and Swirl Tubes: Principles, Design and Operation, second ed. Springer.
Hreiz, R., Gentric, C., Midoux, N., 2011. Numerical investigation of swirling flow in cylindrical cyclones. Chem. Eng. Res. Des. 89, 2521–2539.
Hreiz, R., Lainé, R., Wu, J., Lemaitre, C., Gentric, C., Fünfschilling, D., 2014a. On the effect of the nozzle design on the performances of gas–liquid cylindrical cyclone separators. Int. J. Multiphas. Flow 58, 15–26.
Hreiz, R., Gentric, C., Midoux, N., Lainé, R., Fünfschilling, D., 2014b. Hydrodynamics and velocity measurements in gas–liquid swirling flows in cylindrical cyclones. Chem. Eng. Res. Des. 92, 2231–2246.
Hsiao, T.C., Huang, S.-H., Hsu, C.-W., Chen, C.-C., Chang, P.-K., 2015. Effects of the geometric configuration on cyclone performance. J. Aerosol Sci. 86, 1–12.
Huang, L., Deng, S., Chen, Z., Guan, J., Chen, M., 2018. Numerical analysis of a novel gas-liquid pre-separation cyclone. Separ. Purif. Technol. 194, 470–479.
Ishii, M., Grolmes, M.A., 1975. Inception criteria for droplet entrainment in two-phase concurrent film flow. AIChE J. 21, 308–318.
Jia, J., Wang, M., Schlaberg, H.I., Li, H., 2010. A novel tomographic sensing system for high electrically conductive multiphase flow measurement. Flow Meas. Instrum. 21, 184–190.
Jia, J., Wang, M., Faraj, Y., Wang, Q., 2015. Online conductivity calibration methods for EIT gas/oil in water flow measurement. Flow Meas. Instrum. 46, 213–217.
Kolla, S.S., Mohan, R.S., Shoham, O., 2016. Experimental investigation of liquid carry-over in GLCC© separators for 3-phase flow. ASME International Mechanical Engineering Congress and Exposition, American Society of Mechanical Engineers. V007T009A006.
Kouba, G.E., Shoham, O., Shirazi, S., 1995. Design and performance of gas-liquid cylindrical cyclone separators. In: Proceedings of the BHR Group 7th International Meeting on Multiphase Flow, Cannes, France, pp. 307–327.
Kristoffersen, T.T., Holden, C., Egeland, O., 2017a. Feedback linearizing control of a gas-liquid cylindrical cyclone. IFAC-PapersOnLine 50, 13121–13128.
Kristoffersen, T.T., Holden, C., Skogestad, S., Egeland, O., 2017b. Control-oriented modelling of gas-liquid cylindrical cyclones. In: 2017 American Control Conference (ACC). IEEE, pp. 2829–2836.
Kusters, K.A., Wijers, J.G., Thoenes, D., 1991. Particle sizing by laser diffraction spectrometry in the anomalous regime. Appl. Opt. 30, 4839–4847.
Mao, X., Xie, Q., Duan, Y., Yu, S., Liang, X., Wu, Z., et al., 2020. Predictive models for characterizing the atomization process in pyrolysis of methyl ricinoleate. Chin. J. Chem. Eng. 28, 1023–1028.
Marti, S., Erdal, F., Shoham, O., Shirazi, S., Kouba, G., 1996. Analysis of gas carry-under in gas-liquid cylindrical cyclones. In: Hydrocyclones 1996 International Meeting, St. John College, Cambridge, England, April, Citeseer, pp. 2–4.
Mikheev, N., Saushin, I., Paereliy, A., Kratirov, D., Levin, K., 2018. Cyclone separator for gas-liquid mixture with high flux density. Powder Technol. 339, 326–333.
Molina, R., Wang, S., Gomez, L.E., Mohan, R.S., Shoham, O., Kouba, G., 2008. Wet gas separation in gas-liquid cylindrical cyclone separator. J. Energy Resour. Technol. 130.
Moncayo, J.A., Dabirian, R., Mohan, R.S., Shoham, O., Kouba, G., 2018. Foam break-up under swirling flow in inlet cyclone and GLCC©. J. Petrol. Sci. Eng. 165, 234–242.
Niknam, P.H., Mortaheb, H., Mokhtarani, B., 2018. Dehydration of low-pressure gas using supersonic separation: experimental investigation and CFD analysis. J. Nat. Gas Sci. Eng. 52, 202–214.
Saieed, A., Pao, W., Hashim, F.M., 2018. Effect of T-junction diameter ratio on stratified-wavy flow separation. J. Nat. Gas Sci. Eng. 51, 223–232.
Sanmiguel, I.M., 1998. Bubble Trajectory Analysis in Gas-Liquid Cylindrical Cyclone Separators. University of Tulsa.
Saushin, I.I., Goltsman, A.E., Salekhova, I.G., 2019. Drop entrainment in two-phase non concurrent film flow. In: Journal of Physics: Conference Series, p. 12098.
Singh, B.K., Quiyoom, A., Buwa, V.V., 2017. Dynamics of gas–liquid flow in a cylindrical bubble column: comparison of electrical resistance tomography and voidage probe measurements. Chem. Eng. Sci. 158, 124–139.
Wang, S., 2000. Dynamic Simulation, Experimental Investigation and Control System Design of Gas-Liquid Cylindrical Cyclone Separators, Citeseer.
Wang, S., Gomez, L., Mohan, R., Shoham, O., Kouba, G., Marrelli, J., 2010. The state-of-the-art of gas-liquid cylindrical cyclone control technology: from laboratory to field. J. Energy Resour. Technol. 132, 032701.
Yang, L., Xu, J., 2017. An experimental study on gas and liquid separation at Y-junction tubes by pressure control. Separ. Sci. Technol. 52, 1496–1503.
Yang, L., Zhang, J., Ma, Y., Xu, J., Wang, J., 2020a. Experimental and numerical study of separation characteristics in gas-liquid cylindrical cyclone. Chem. Eng. Sci. 214, 115362.
Yang, L., Zou, L., Ma, Y., Wang, J., Xu, J., 2020b. Breakup, coalescence, and migration regularity of bubbles under gas–liquid swirling flow in gas–liquid cylindrical cyclone. Ind. Eng. Chem. Res. 59, 2068–2082.
Yin, J., Li, J., Ma, Y., Wang, D., 2016. Numerical approach on the performance prediction of a gas–liquid separator for TMSR. J. Nucl. Sci. Technol. 53, 1134–1141.
Yin, J., Qian, Y., Zhang, T., Wang, D., 2019. Measurement on the flow structure of a gas-liquid separator applied in TMSR. Ann. Nucl. Eng. 126, 20–32.
Yue, T., Chen, J., Song, J., Chen, X., Wang, Y., Jia, Z., Xu, R., 2019. Experimental and numerical study of upper swirling liquid film (USLF) among gas-liquid cylindrical cyclones (GLCC). Chem. Eng. J. 358, 806–820.
Zhang, J., Xu, J.Y., 2016. Rheological behaviour of oil and water emulsions and their flow characterization in horizontal pipes. Can. J. Chem. Eng. 94, 324–331.